Comparative analysis of shape defects induced by the micro-machining of glassy polymers

Faissal Chegdani[a,*], Mohamed El Mansori[a,b], Stéphane Bessonnet[c], Sébastien Pinault[c]

[a] Arts et Métiers Institute of Technology, MSMP, HESAM University, F-51006 Châlons-en-Champagne, France.
[b] Texas A&M Engineering Experiment Station, College Station, TX 77843, USA.
[c] ESSILOR International, 63 Boulevard Jean-Baptiste Oudry, 94000 Créteil, France.

ABSTRACT

This paper aims to investigate the cutting behavior of optical glassy polymers in order to identify the shape defects induced by the micro-machining processes. Polycarbonate (PC), Allyl Diglycol Carbonate (CR39), and polythiourethane (MR7) polymers are considered in this study to perform micro-machining experiments using the orthogonal cutting configuration. The comparative analysis is carried out by conducting the cutting experiments on hybrid samples that are composed of two types of polymers (MR7-PC, CR39-PC, and MR7-CR39), and then comparing the topographic state of the machined hybrid surfaces. Results show that PC is by far the polymer that generates the most shape defects because of its high rate of spring-back. This finding has been validated by nanoindentation experiments that reveal the highest mechanical reaction of PC at the time of nanoindentation unloading. This study demonstrates also that the measured thrust forces could be an indicator for predicting the spring-back defects induced by micro-machining.

KEYWORDS

Glassy polymers; Micro-machining; Shape defects; Spring-back; Thrust force; Nanoindentation.

[*] Corresponding author: faissal.chegdani@ensam.eu

1. Introduction

The manufacturing and development of glassy polymers for optical applications have gained the interest of academia and industries for many decades to replace mineral glasses. Indeed, despite their inherent advantages like high wear and abrasion resistance, excellent optical properties, high durability, and acceptable cost, silicate glasses show disadvantages such as high weight and brittleness, which can be uncomfortable and possibly dangerous for customers [1]. Optical polymers can counter these issues and have been introduced to the optical industry after the Second World War through the Allyl Diglycol Carbonate (ADC) commonly known as CR39 [2]. CR39 is a transparent, thermosetting resin that combines an exceptional range of qualities not available in all plastic materials [3]. From 1955, polycarbonate (PC), a very tough thermoplastic polymer, started to be developed for optical application and it became widely available by the late 1980s [2]. Then, the research progress led to the development of polythiourethane (commonly known as MR7) in 1991 by the Mitsui Company in Japan [4,5]. MR7 is a thermoset transparent polymer with a higher refractive index of 1.67.

Optical applications such as spectacle lenses require shaping with very high precision in order to properly match the visual needs of customers. Therefore, micro-machining is mandatory in the manufacturing process of optical products to ensure micro-accuracy in shape and dimensions. Micro-machining processes remain challenging because they exhibit different issues such as the poor cutting contact stiffness leading to a tool breakage [6], the difficulty of adding tool coating due to the significant increase of the cutting edge radius [7], and the size effect [8]. The micro-machining process of optical lenses is usually performed using the diamond turning technique to meet the accuracy requirements [9–12]. However, if the process parameters are not adapted to

the work-material properties, micro-shape defects can be induced and, consequently, the optical performances of the resulting lens may not meet the required optical specifications, leading to its rejection. In micro-machining, micro-shape defects can occur from many origins, among which one finds the spring-back of the work-material that results from unfavorable cutting conditions when the depth of cut is below or up to a minimum critical value that is called the minimum chip thickness [13,14]. This critical minimum chip thickness depends mainly on the work-material properties, the cutting edge radius, and the process parameters [15]. Indeed, it has been shown for steel and soft polymers that plowing and elastic recovery occur instead of cutting if the uncut chip thickness is less than the cutting edge radius [16,17].

In the case of glassy polymers, the polymer can be thermoplastic (such as PC) or thermoset (such as CR39 and MR7) which implies an important difference in the thermomechanical properties of the work-material. Indeed, thermoplastic polymers are mechanically sensitive to temperature and show ductile behavior at failure in the vicinity of their glass transition temperature [18]. On the other side, the heavily crosslinked networks of thermoset resins after polymerization make them less sensitive to temperature and are usually characterized by a brittle behavior at failure [18]. These differences could significantly modify the cutting behavior, the cutting mechanisms, and the induced shape defects during micro-machining in the function of the polymer type. Therefore, the parameterization of the machining process cannot be the same for these three polymers and the micro-shape defects that could be induced in each polymer must be quantified to be able to put them under control within the industrial production line. The literature does not provide works dealing with the quantification of the machining-induced shape defects of optical polymers, which

represents a lack of scientific data to develop a harmonized machining system suitable for the manufacturing of different optical polymers used in the industry.

Hence, this paper proposes an experimental analysis that allows comparing the cutting behavior of PC, CR39, and MR7 with a quantitative assessment of the machining-induced micro-shape defects. Orthogonal cutting configuration is considered in this study with a polycrystalline diamond (PCD) cutting insert. Cutting experiments are conducted on three hybrid samples composed of two different polymers, and the assessment of micro-shape defects is performed with topographic measurements of the machined hybrid surfaces. Cutting and thrust forces have been measured to assess the tool/material interactions depending on the cutting conditions. The chip morphology has been investigated through the in-situ observation of chip formation (using a fast camera) and microscopic analysis of the removed chips (using a scanning electron microscope). To understand and discuss the difference in shape defects between the three polymers, mechanical characterization is carried out at the microscale with nanoindentation using atomic force microscopy (AFM). The experimental approach is described in detail in the next section.

2. Experimental approach

2.1. Hybrid samples preparation

PC, CR39, and MR7 materials have been provided as semi-finished workpieces in the form of thick disks (Figure 1(a)). Table 1 presents some physical properties of the optical polymers considered in this study. Each semi-finished workpiece has been milled to obtain rectangular samples with the dimensions of 80×10×3 mm. Hybrid workpieces for orthogonal cutting experiments are obtained by gluing two different polymer samples (Figure 1(b)) to get three different hybrid configurations for micro-

machining experiments as shown in Figure 1(c): MR7-PC, CR39-PC, and MR7-CR39. In each hybrid sample configuration, the polymer with the higher elastic modulus (from Table 1) is considered as the reference material.

Table 1: Physical properties of the considered optical polymers [5,19–24]

Optical polymer	Refractive index	Elastic modulus (GPa)	Heat deflection temperature (°C)	Glass transition temperature (°C)
PC	1.59	2.27	142 – 148	150 – 151
CR39	1.5	3.7	84	89 – 112
MR7	1.67	5.9	85	75 – 150

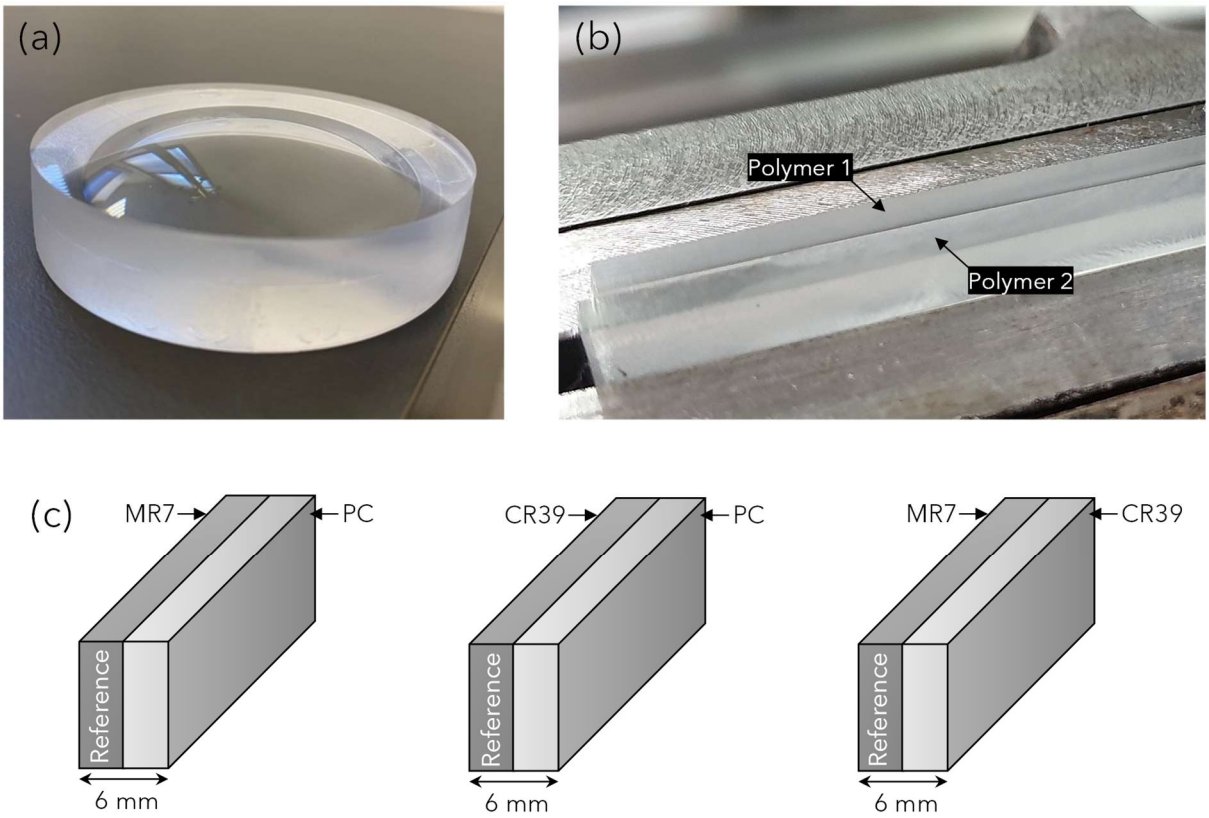

Figure 1: (a) Image of the provided semi-finished optical polymers, (b) Image of hybrid polymer samples used for orthogonal cutting, (c) Schematic depiction of the three hybrid sample configurations

2.2. Orthogonal cutting setup

The orthogonal cutting configuration has been chosen to perform the machining experiments. Orthogonal cutting is mainly used in scientific investigations because it represents the local tool/material contact in the main conventional machining processes. Orthogonal cutting involves the basic physical phenomena that occur during a cutting operation. Moreover, it allows good discrimination of elementary cutting mechanisms regardless of the influence of complex geometries and kinematics of cutting tools in conventional machining processes. Cutting experiments are carried out on a shaper machine (Model GSP – EL 136). As shown in Figure 2, the hybrid workpiece is clamped manually in the machine bearing between two hardened steel plates. Orthogonal cutting of the sample results from the relative motion between the tool, fixed to the moving saddle, and the workpiece.

A piezoelectric dynamometer (Model Kistler – 9255B) is used to capture the force data in the Cartesian coordinate system. The piezoelectric dynamometer has a sensitivity of ≈ -8 pC/N in the feed direction (cutting force direction) and ≈ -3.7 pC/N in the normal to the feed direction (thrust force direction). Data collection is performed via an amplifier (Model Kistler – 5017 B1310) connected to a data acquisition card (Model National Instruments – BNC-2110). Machining forces display is performed with a LabVIEW data recorder program at a sampling rate of 5000 Hz. A high-speed camera (FASTCAM SA5 CCD) was used for recording optical frames of in-situ chip formation at an acquisition rate of 7,000 fps.

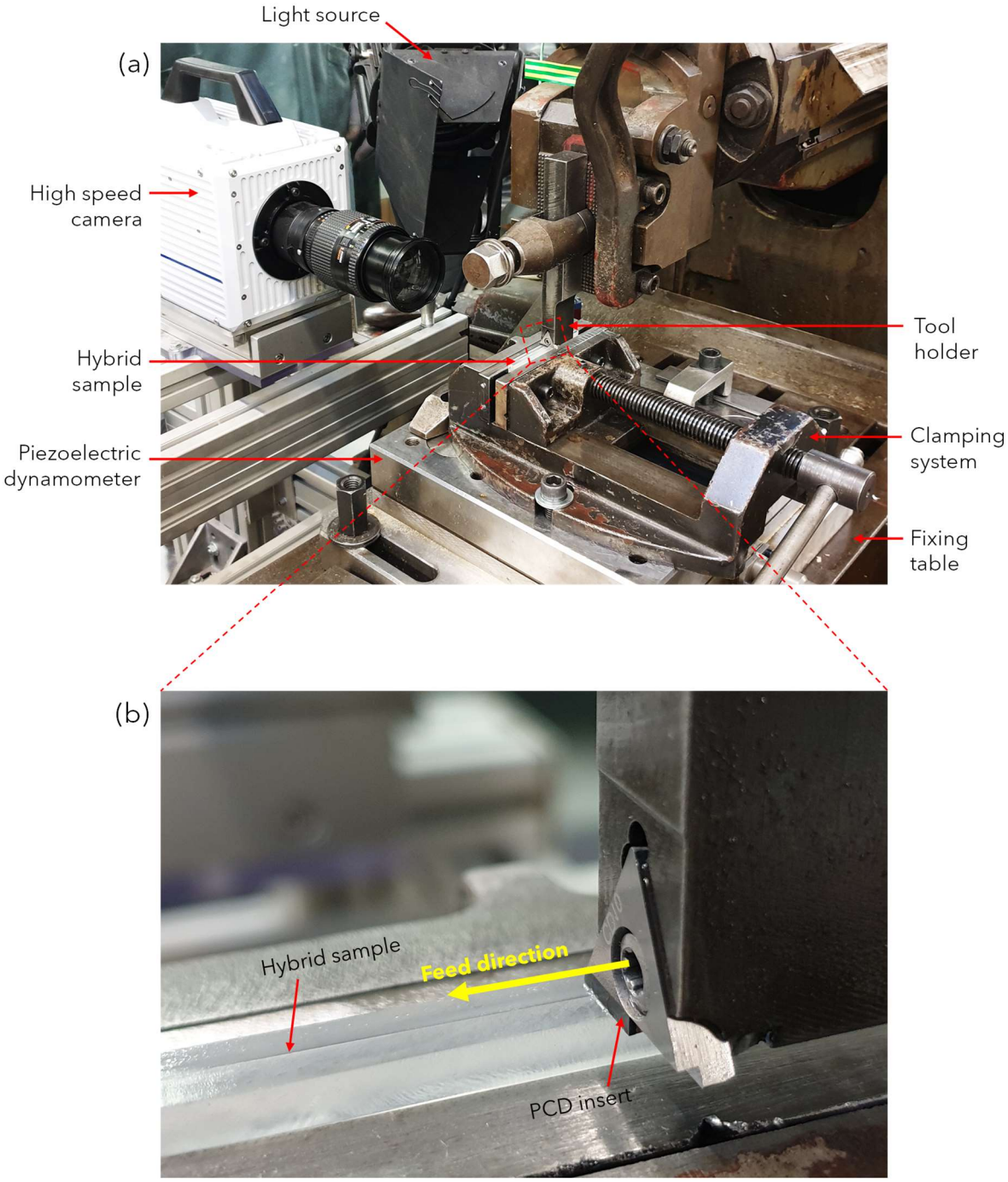

Figure 2: Experimental setup for orthogonal cutting tests with a zoomed view of the active cutting zone

Polycrystalline diamond (PCD) inserts (model Sandvik TCMW16T304FLP-CD10) are used in this study as cutting tools (Figure 2(b)). The choice of this kind of cutting insert is motivated by its high sharpness compared to the other commercial cutting inserts thanks to the PCD microstructure as shown in the SEM image of Figure 3(a). PCD inserts have a rake angle of 0° and a clearance angle of 7°. The cutting edge radius of

the PCD insert has been calculated with an atomic force microscope (AFM) using Tapping mode to obtain topographic measurements of the cutting edge curvature at different locations on the cutting edge. Then, the radius of the curvature is calculated by extracting different 2D profile sections from the 3D surface topography of Figure 3(b). The resulting cutting edge radius is found to be $3.23^{\pm 0.4}$ µm.

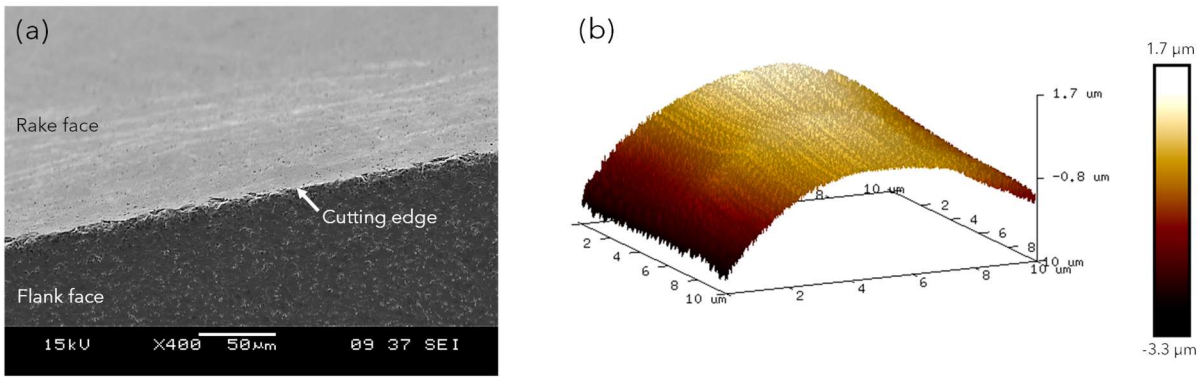

Figure 3: (a) SEM image of the active zone of the PCD insert showing the cutting edge, (b) AFM topographic measurement of the cutting edge curvature to calculate the cutting edge radius

2.3. Assessment method of machining-induced shape defects

The comparative analysis of the machining-induced shape defects has been carried out by comparing the difference in height between the two machined surfaces of the two materials present in the hybrid sample. Three values of cutting speed (8, 20, and 32 m/min) have been considered in this work from the available configurations of the shaper machine. Small cutting depths (between 3 µm and 23 µm) have been chosen in orthogonal cutting experiments to respect the micro-machining configuration. The shaper machine is equipped with an indicator instrument that has a precision level of 10 µm. Therefore, to ensure accuracy at the considered range of cutting depths, the relative effective depth of cut was measured directly from the hybrid machined surface by keeping an initial surface zone on each reference material as shown in the example of Figure 4. Indeed, the hybrid sample is first subjected to edge trimming on the whole worksurface in order to have a flat surface tangent with the cutting edge (Figure 4(a)).

Then, the cutting tool is offset by 1 mm from the reference polymer before performing the cutting operation (Figure 4(b)).

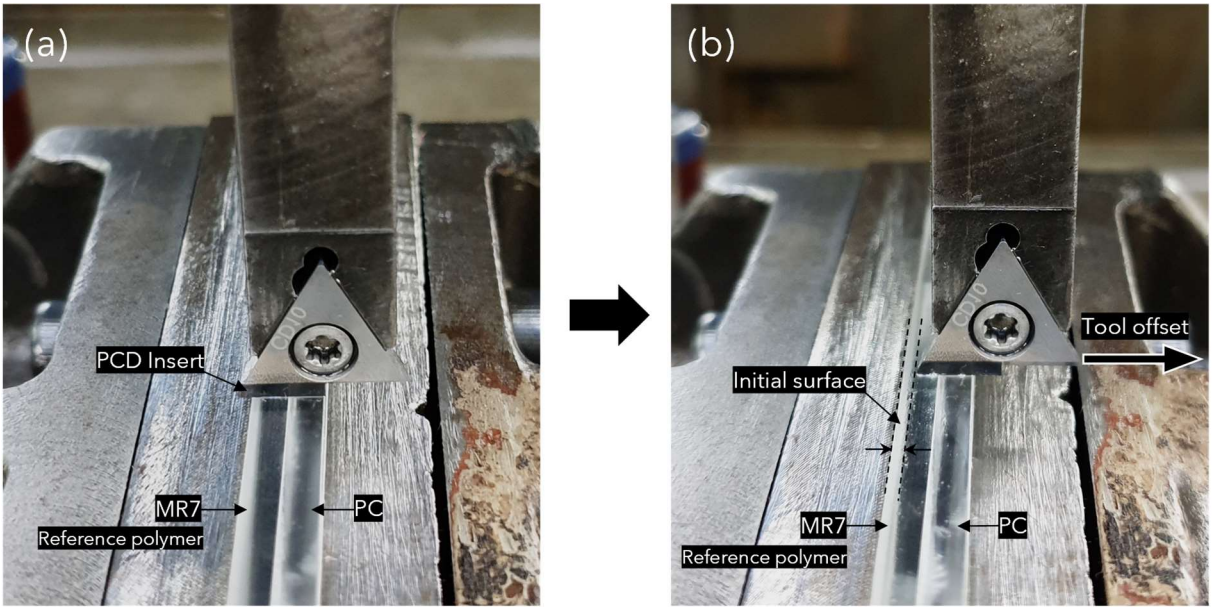

Figure 4: Example of the experimental cutting method with MR7/PC sample. (a) step 1: edge trimming of the whole hybrid worksurface, (b) step 2: orthogonal cutting test with the keeping of an initial surface zone on the reference polymer material

With this cutting configuration, the effective depth of cut relative to the reference material can be determined by measuring the height difference between the initial surface and the machined surface of the reference material. To this aim, topographic measurements on the machined surfaces after performing each orthogonal cutting experiment have been realized using an optical interferometer (model WYKO 3300NT). The stitching mode was used to cover the three characteristic zones of the hybrid surface as shown in the example of Figure 5(a). Then, a 2D profile is extracted from the topographic surface to determine the relative effective depth of cut (a_p) and the relative spring-back defect (Δz) as shown in the example of Figure 5(b). At each cutting experiment, five to six topographic measurements are carried out on the resulting machined surface at different locations from the entry to the exit of the sample length in order to verify the repeatability.

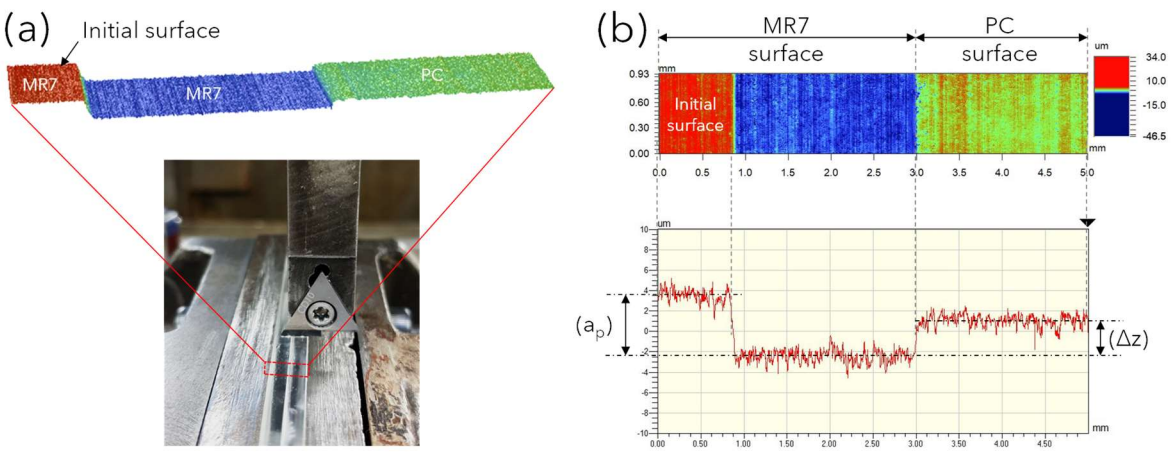

Figure 5: Example of topographic measurements on machined surfaces with MR7/PC samples. (a) 3D view, and (b) 2D view with the extraction of the profile for measuring the relative effective depth of cut (a_p) and the relative spring-back defect (Δz)

2.4. Nanoindentation measurements

The nanoindentation technique has been widely used to measure the mechanical properties of materials at the microscale [19,25,26]. In this study, the objective of nanoindentation measurements is to investigate the mechanical reaction of each optical polymer to the solicitation of the tip indenter for the purpose of understanding and discussing the results of micro-machining experiments. To this aim, an atomic force microscope (AFM - Dimension Edge™ - Bruker) has been used with a Berkovich diamond tip indenter (Bruker DNISP-HS) that has a stainless-steel cantilever with a spring constant of 450 N/m and tip radius of 40 nm. As shown in Figure 6(a), optical polymers are embedded in epoxy resin and polished to have a nano-smoothed surface for AFM scanning.

Nanoindentation involves the normal contact of an indenter on a worksurface and its penetration in this surface to a specified load or depth [27] (Figure 6(b)). The load is measured regarding the displacement into the worksurface to get the load–penetration curve shown in Figure 6(c). In this study, the contact stiffness (“S” in Figure 6(c)), which is the slope of the tangent line to the unloading curve at the maximum loading, is used

to characterize the mechanical reaction of each optical polymer. With this nanoindentation procedure, “S” represents the mechanical elastic reaction of the indented material after the plastic deformation occurred during the indentation loading.

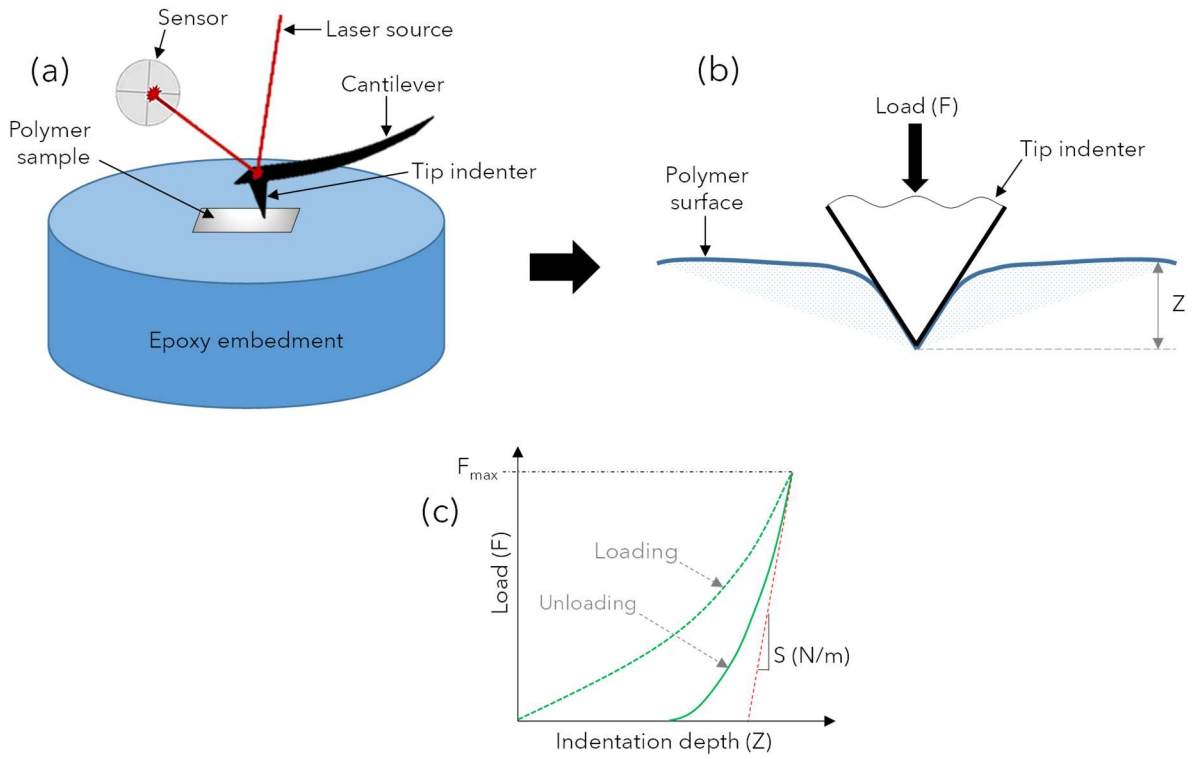

Figure 6: (a) Schematic illustration of the experimental setup for nanoindentation measurements using atomic force microscope, (b) Schematic illustration of the nanoindentation process showing the indentation depth, and (c) Typical Loading/unloading curve obtained from nanoindentation

3. Results and discussion

3.1. Analysis of chip formation

Before analyzing the chip formation of hybrid polymer samples, an observation of the chip morphology of each polymer separately was carried out to determine the intrinsic cutting behavior of each material. Figure 7 shows the in-situ chip formation of PC, CR39, and MR7 where the cutting speed has been fixed at 20 m/min and the depth of cut has been set to 15 µm. At this level of cutting depth, PC generates a continuous and curled chip (Figure 7(a)), while CR39 shows a fragmentation of the chip that has a form of debris (Figure 7(b)). In the case of MR7, the chip seems to be continuous.

However, the MR7 chip does not curl and remains in contact with the rake face (Figure 7(c)).

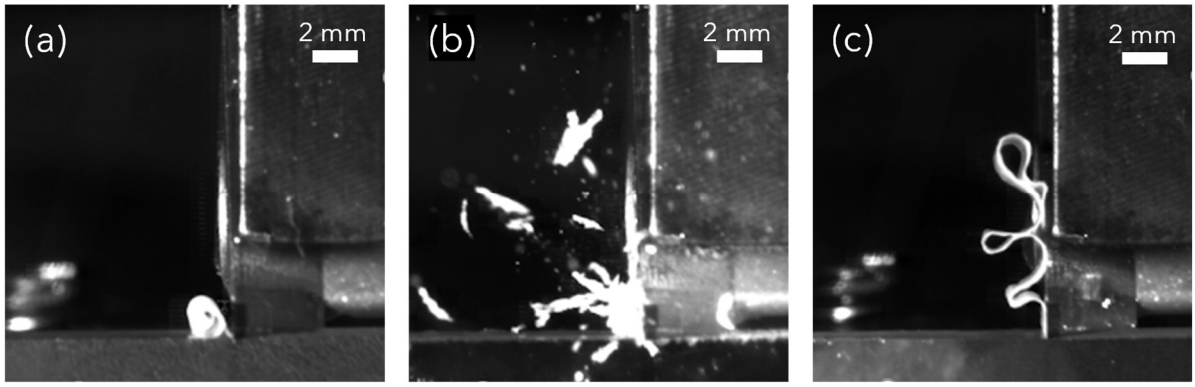

Figure 7: High-speed camera images showing the chip formation during the cutting of (a) PC, (b) CR39, and (c) MR7

The chip formed by PC is well-known as a shear-flow type chip that is obtained by a ductile chip formation process and is caused by plastic deformation of the material as it passes through a shear plane at the primary shear zone [28]. The chip curling of PC belongs to the important plastic deformation at the secondary shear zone, especially because of the cutting-induced temperature since the mechanical properties of thermoplastic polymers are highly sensitive to temperature as explained in section 1. On the other hand, the thermoset origin of CR39 leads to a brittle chip formation process and a high brittle breakage rate of the chip to form debris [28].

However, despite the thermoset origin of MR7, a continuous chip seems to be formed without curling which is not conventional. Indeed, polythiourethane thermoset polymers exhibit a ductile behavior due to their crystalline nature that results in superior toughness, which is in sharp contrast to the brittleness of typical thermoset polymers such as epoxy [29]. The chemical reason behind this behavior could be linked to the fact that glassy polymers of low molar mass have little cohesive strength, leading to a brittle behavior, while glassy polymers of high molar mass are characterized by long chains that form a network due to their uncrossability and prevent brittle failure during

large deformation [30]. The molar mass of polythiourethane is around 35000 g/mol [31]. This value is highly greater than the molar mass value of CR39 which is around 274 g/mol [32] (near to the molar mass of epoxy which is around 392 g/mol [33]). This could explain the ductile behavior of MR7 and the brittle behavior of CR39 (which is similar to the well-known behavior of epoxy resin).

To a better understanding of the chip formation behavior, especially for MR7, Figure 8 shows microscopic images of the removed chips of PC, CR39, and MR7 obtained using a scanning electron microscope (Model JEOL – 5510LV) with a low vacuum mode. The three considered polymers reveal different morphologies on their removed chips. The surface of the PC chip shows a smooth state with traces of surface plastic deformation at the microscale (Figure 8(a)), which is the general case of thermoplastic polymers. The microscopic observation of the fragmented chips of CR39 shows a neat surface with micro-cracks that are a sign of a brittle failure during the chip formation process (Figure 8(b)). In the case of MR7, Figure 8(c) reveals a segmented chip that is formed with periodic waved-shape lamellae. This chip formation process is similar to that shown in literature for titanium [34–37] and was attributed to the heterogeneous plastic deformation that occurs at the microscale during the cutting process [38]. This heterogeneous plastic flow is responsible for the lamellar structure of the chip, which is explained by the variation in the deformation process that causes the creation of concentrated shear bands [39].

As shown at the microscale in Figure 8(c), the lamellar structure generated in the MR7 chip induces damage in the form of micro-cracks between the periodic waved-shaped lamellae. This damage weakens the structural integrity of the chip, preventing its curl.

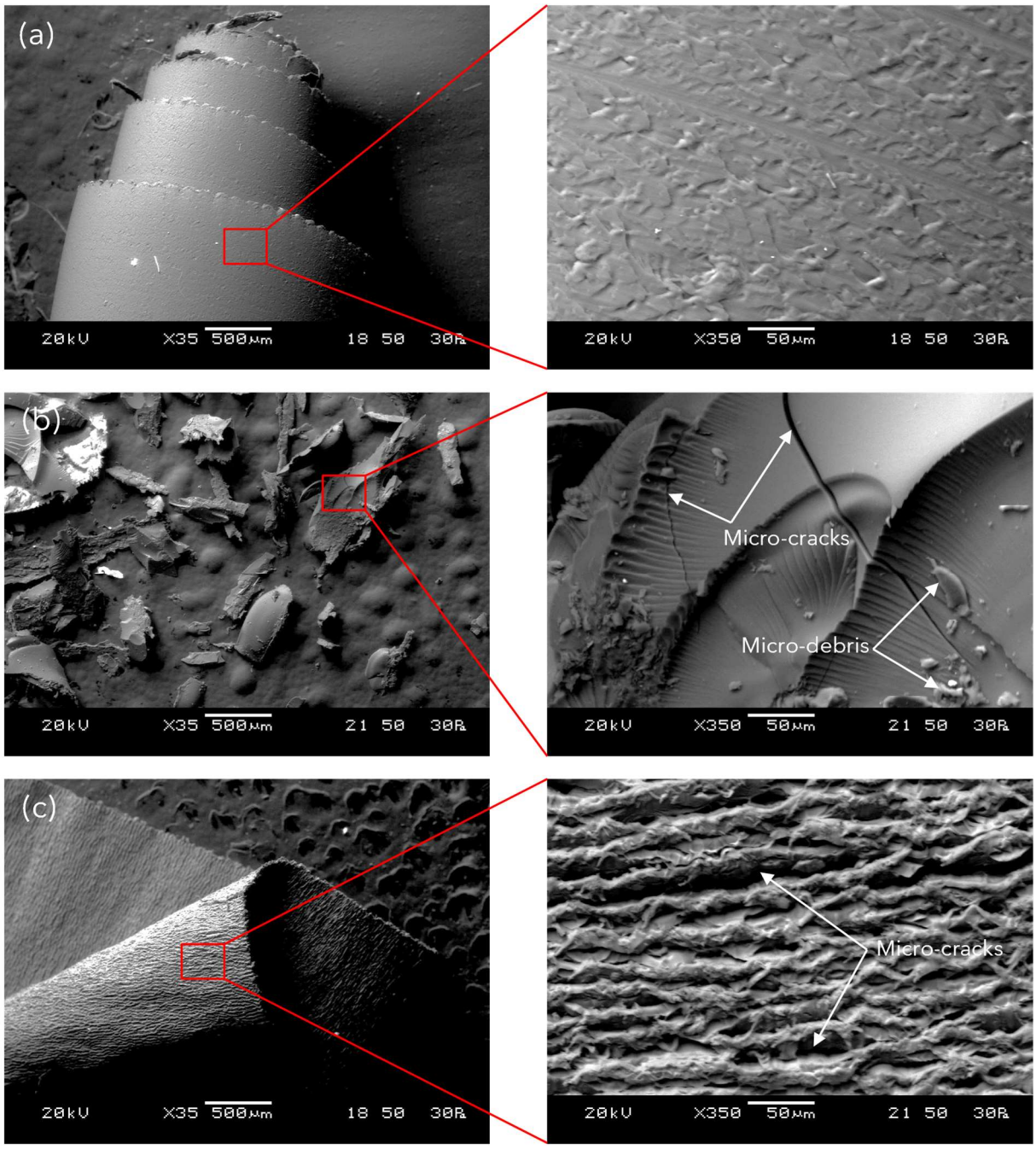

Figure 8: SEM images of the removed chips showing their microscopic morphology. (a) PC, (b) CR39, and (c) MR7

In the case of hybrid polymer samples, Figure 9 shows that the discontinuous structure of the CR39 chip does not affect the chip formation of the hybrid samples (Figure 9(b),(c)), while the presence of MR7 leads to reducing the chip curl of PC (Figure 9(a)). It can be also noticed in Figure 9(a) a whitening of the MR7 chip compared to the PC

chip that remains transparent as the initial state shown in Figure 4. This is a sign of damage in the MR7 chip due to the lamellar structure formation.

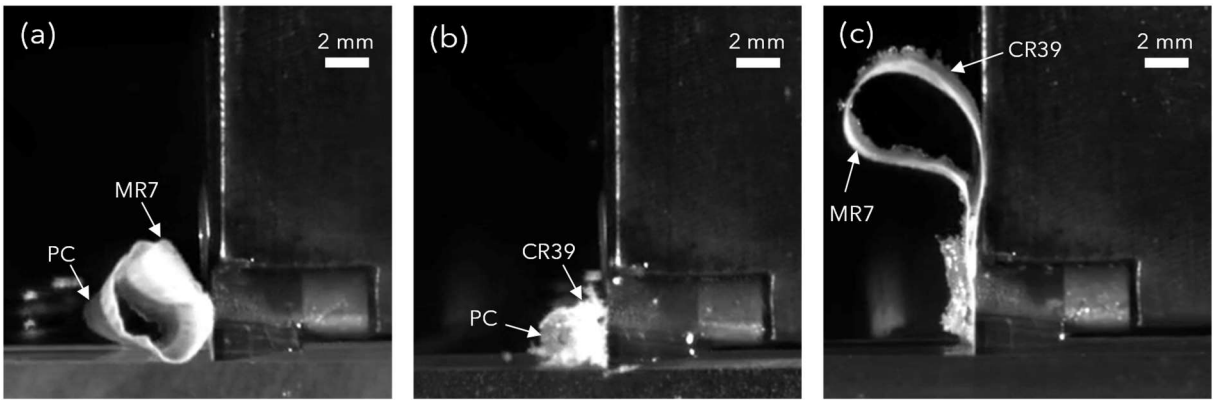

Figure 9: High-speed camera images showing the chip formation of hybrid samples during the cutting of (a) MR7-PC, (b) CR39-PC, and (c) MR7-CR39

3.2. Analysis of micro-machining forces

Figure 10 shows the cutting forces (Fc) that were measured in the cutting feed direction. For all the cutting configurations, the increase in the depth of cut leads to an increase in the cutting force which is a well-known behavior. MR7-PC samples generated the highest cutting forces, followed by MR7-CR39 and CR39-PC. The difference is more relevant when approaching the highest values of cutting depths. No significant effect is observed on cutting forces when increasing the cutting speed from 8 m/min to 32 m/min. Introducing MR7 on the hybrid samples contributes to an increase in the cutting forces due to its higher elastic modulus compared to the other materials (cf. Table 1). The contribution of MR7 to the cutting forces is more relevant with PC since the chip remains continuous as shown in section 3.1.

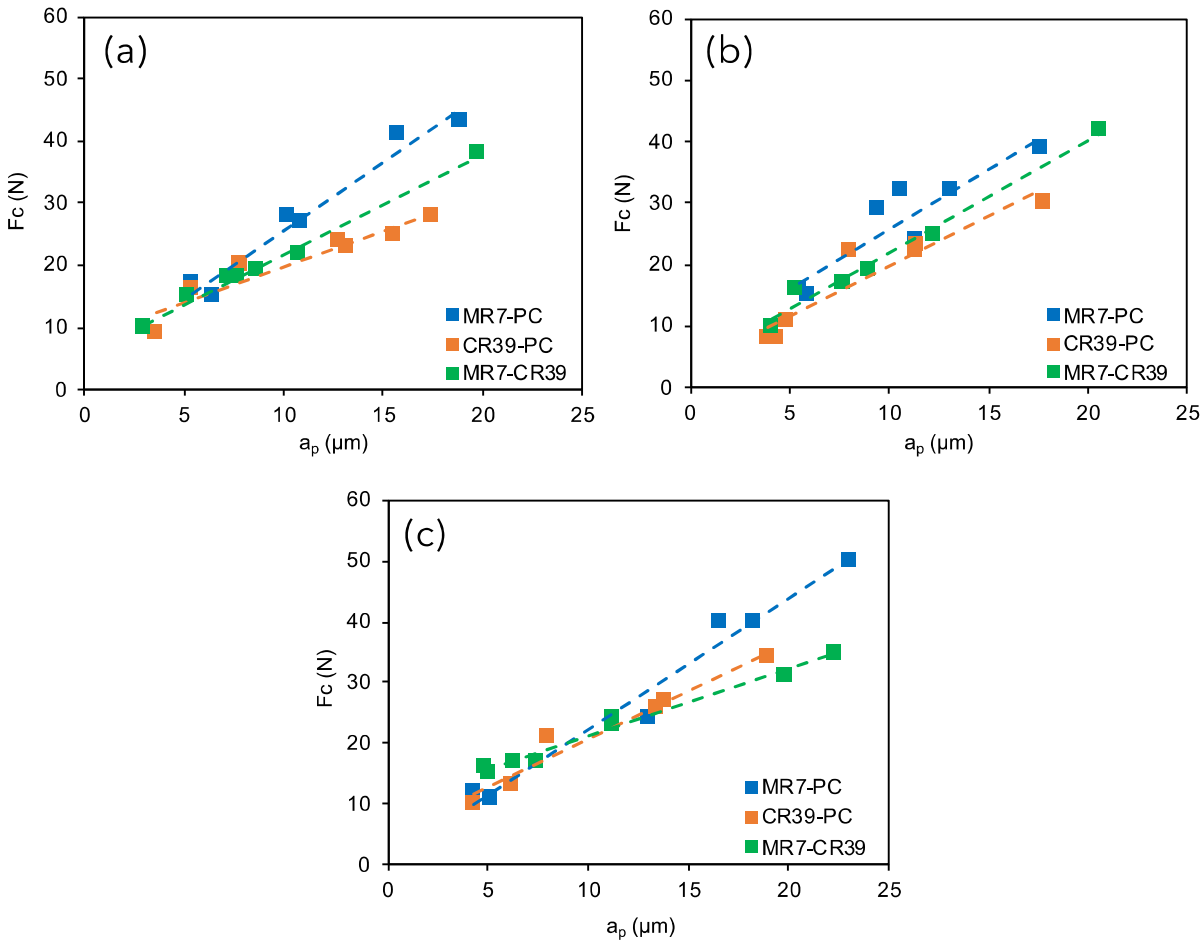

Figure 10: Cutting forces of hybrid polymer samples with (a) Vc = 8 m/min, (b) Vc = 20 m/min, and (c) Vc = 32 m/min

Figure 11 presents the thrust forces (Ft) that were measured perpendicularly to the cutting feed direction. MR7-PC shows the highest values of thrust forces that decrease with the increase of the cutting depth. The same behavior is noticed for the thrust force of CR39-PC samples. However, the trust forces of MR7-CR39 are not affected by the variation of the cutting depth at the considered range from 3 µm to 23 µm. A slight increase in the thrust forces is observed when increasing the cutting speed.

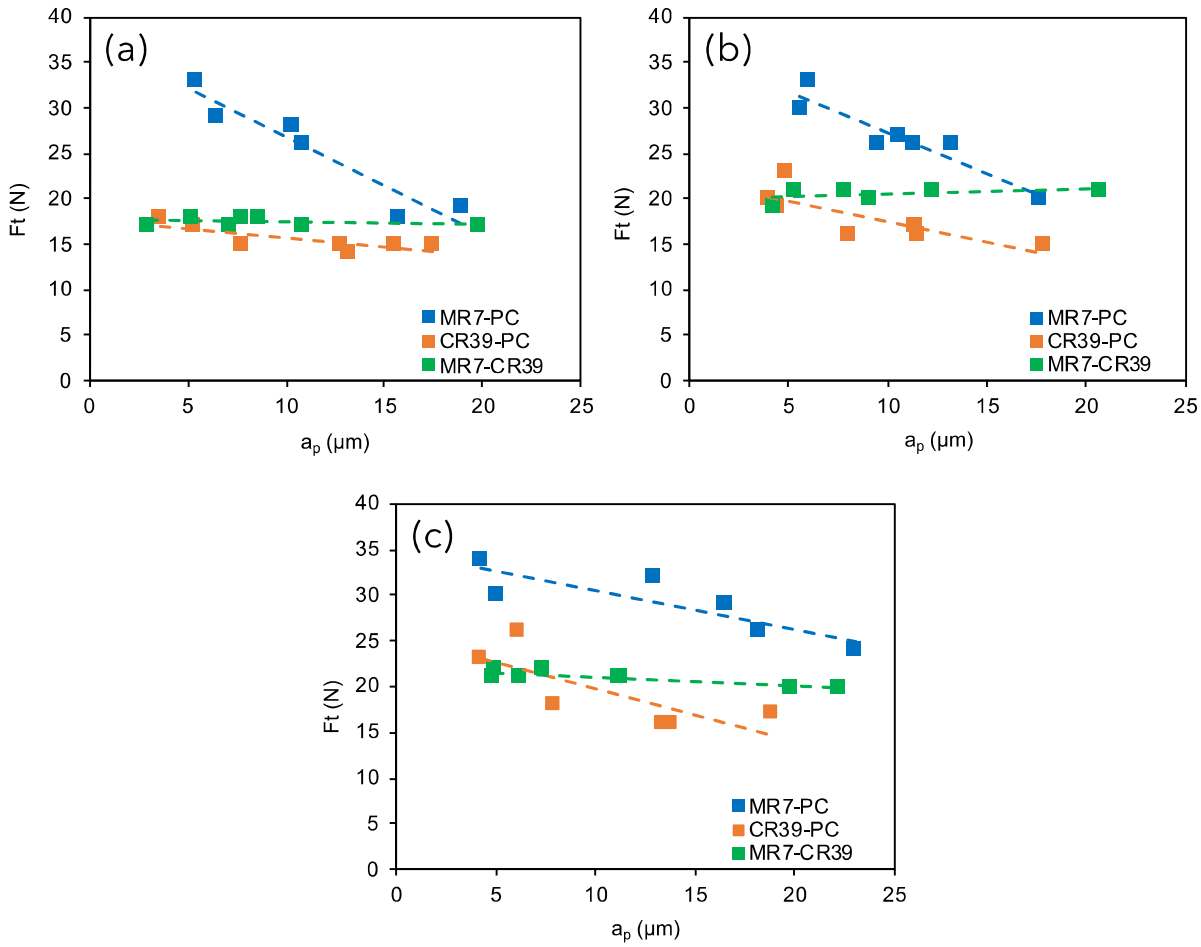

Figure 11: Thrust forces of hybrid polymer samples with (a) Vc = 8 m/min, (b) Vc = 20 m/min, and (c) Vc = 32 m/min

Figure 11 leads to the conclusion that introducing PC in hybrid samples contributes to an important increase in thrust forces, particularly when approaching the lowest values of cutting depth. This means that the normal mechanical reaction between the cutting tool and the PC is intensified at low cutting depths. This behavior of PC could be due to an elastic recovery when the depth of cut is below or up to the critical minimum chip thickness as explained in section 1. This aspect is investigated in depth in the next section.

3.3. Analysis of the relative spring-back defects

Figure 12 presents the relative spring-back (Δz) measured between the two machined surfaces of the hybrid samples as described in section 2.3. It can be seen that the PC generates the highest Δz. The PC spring-back regarding MR7 is higher than that regarding CR39. However, Δz of PC shows a significant decrease in the function of the cutting depth. The CR39 spring-back regarding MR7 has the lowest values and is not significantly affected by the depth of cut variation. Hence, at the highest values of cutting depth (~ 17 – 20 µm), the Δz of the three hybrid samples become almost similar. The increase in the cutting speed leads to a slight increase of Δz for the three hybrid samples.

Reducing the depth of cut increases significantly the PC spring-back regarding MR7 and CR39. Based on the results of Figure 12, at a relative depth of cut of ~ 5 µm, Δz of PC represents ~ 70% of the corresponding cutting depth in MR7, and ~ 55% of the corresponding cutting depth in CR39. These results demonstrate that PC is characterized by a high elastic recovery compared to MR7 and CR39, which is in total agreement with the results of thrust forces shown in Figure 11 where introducing PC in hybrid samples contributes to a significant increase in the thrust force, especially at low cutting depths. Indeed, the increase in the thrust force during cutting means an intensification of the normal mechanical reaction of the work-material against the contact with the cutting tool, which could strongly be induced by the elastic recovery of the work-material.

It can be concluded that the critical minimum chip thickness required for material removal of PC is significantly higher than that of CR39 and MR7. This behavior puts the PC in unfavorable cutting conditions at an early stage in micro-machining, which could strongly induce micro-shape defects in the case of superfinishing processes

because the effectively removed thickness is different from the required thickness to remove.

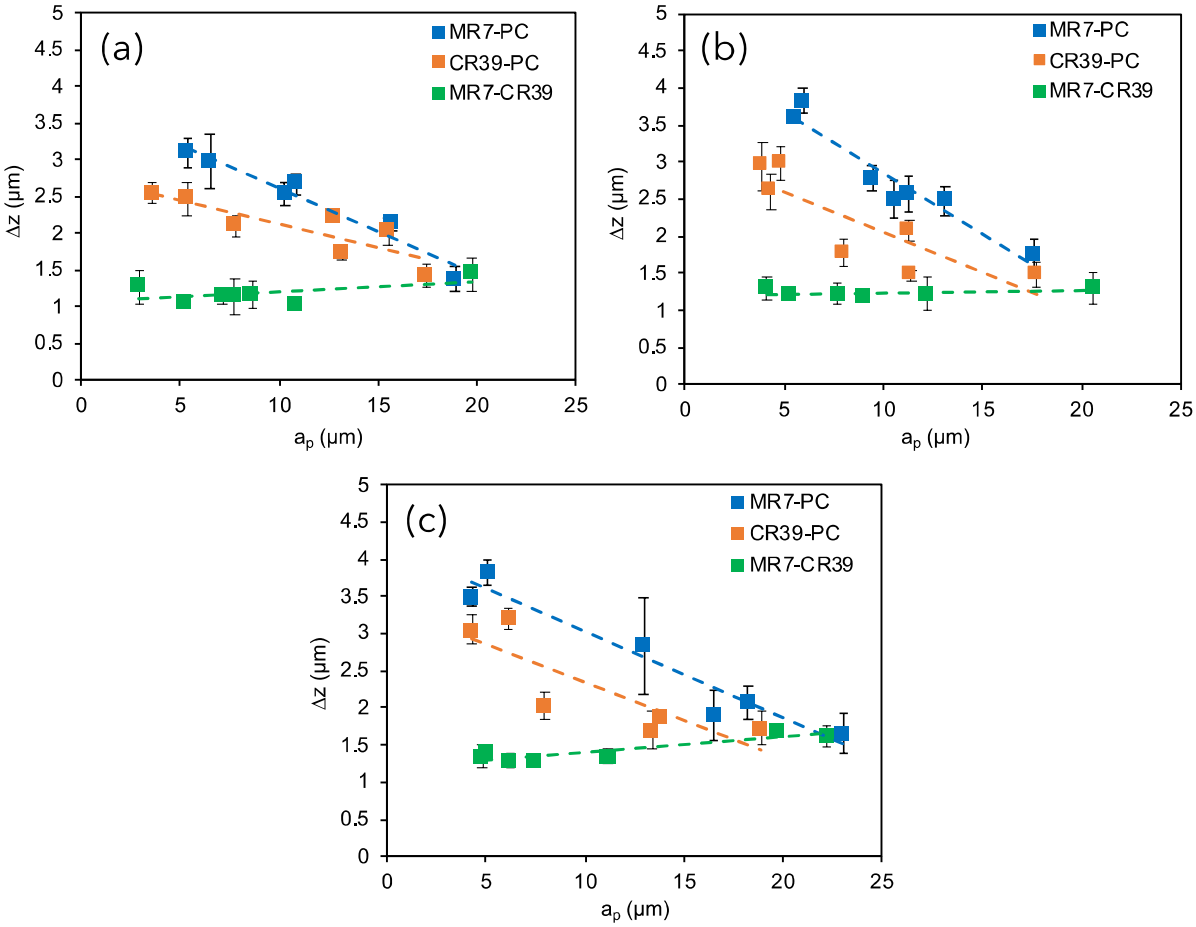

Figure 12: Relative spring-back in hybrid polymer samples with (a) Vc = 8 m/min, (b) Vc = 20 m/min, and (c) Vc = 32 m/min

CR39 generates also a spring-back regarding MR7 which is between 1 µm and 1.5 µm at the considered range of cutting depth. This indicates that MR7 has the lower critical minimum chip thickness required for material removal. However, it is important to note that MR7 could also show a relative spring-back if it has been compared with another material that has a lower elastic recovery at this range of cutting depth. To validate the hypothesis of the elastic recovery as the origin of the difference in cutting behavior between the three polymers, the next section will address their mechanical reaction with nanoindentation.

3.4. Analysis of the mechanical response using AFM nanoindentation

Figure 13 shows the indentation traces performed on each optical polymer. It can be seen that the three polymers do not have the same mechanical reaction during the nanoindentation contact. Indeed, at similar indentation depths, the indentation traces of the three polymers do not have similar sizes. PC shows the highest sizes and the deepest indentation traces at the considered range of indentation depth. At low depths, MR7 shows the smallest sizes of indentation traces due to its higher stiffness compared to the other considered polymers. However, by increasing the depth up to 4 µm, the size of indentation traces becomes similar to that of PC. This indicates an important plastic deformation of MR7 despite its thermoset origin, which is due to its important chemical crosslinking chains induced by its higher molar mass as described in section 3.1. CR39 generates the lowest sizes of indentation traces, especially at high depths. Moreover, the indentation traces of CR39 are not as deep as those of MR7 and PC because MR7 induces higher plasticity than CR39. This confirms the origin of the continuous chip observed for MR7 in Figure 7.

It can be concluded from this analysis of indentation traces that PC generates the highest plastic deformation even with small indentation depths, while the plastic deformation of MR7 is activated by increasing the depth of indentation. CR39 shows the lowest plasticity, which is in good agreement with the experimental observation of chip formation in section 3.1.

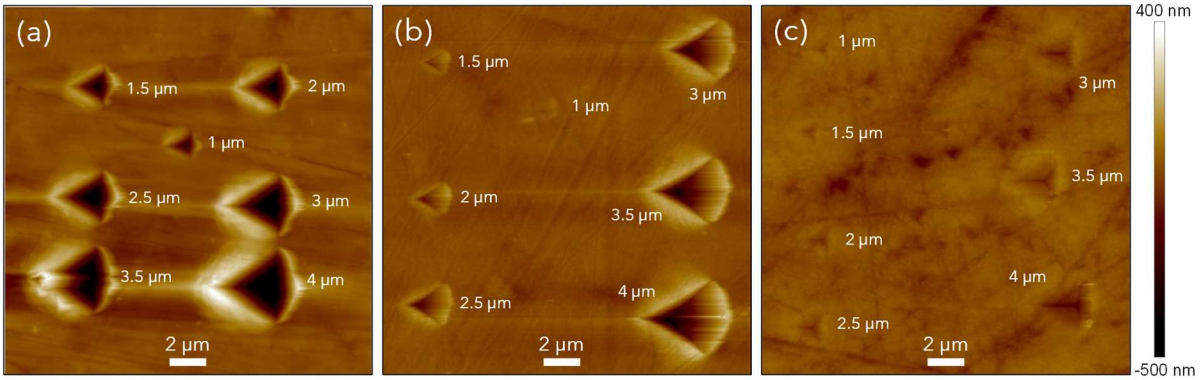

Figure 13: AFM scanning images of the indentation traces performed on (a) PC, (b) MR7, and (c) CR39. In each image, the corresponding indentation depth is mentioned near each indentation trace

Figure 14 presents typical loading-unloading curves obtained from the nanoindentation of PC, MR7, and CR39. Results of Figure 14 show that PC induces the highest indentation force at all the considered range of the indentation depth. MR7 generates the lowest force at low indentation depth (Figure 14(a),(b)). However, the increase in indentation depth leads to a significant increase in the indentation force of MR7 to be equal to or slightly higher than that of CR39 from 3 µm of indentation depth (Figure 14(c),(d)). It can also be noticed a change in the loading/unloading behavior in the function of the indentation depth. At low applied depths, the loading force shows a quasi-linear behavior in the function of the indentation depth after a slight non-linear zone that corresponds to the tip engagement on the work-material. Then, the unloading force curve deviates from the loading curve with a higher slope ("S" in Figure 6(c)) than that of the loading curve (Figure 14(a)). When increasing the applied depth, the loading and unloading curves reveal a non-linear behavior in the function of the indentation depth, especially at the maximum applied depth of 4 µm as shown in Figure 14(d). Moreover, it can be observed that the increase of the applied depth leads to reducing the deviation between the loading and the unloading curve by the decrease of the slope of the unloading curves from the maximum force "S". Reducing "S" could be associated to a decrease of the reaction force from the work-material to the tip indenter generated

by the elastic recovery after the plastic deformation during the nanoindentation process. This phenomenon may be similar to that of material spring-back observed during orthogonal cutting in the function of the depth of cut. Therefore, the unloading slope “S” related to each glassy polymer is calculated in Figure 15(a) in the function of the applied indentation depth. It can be seen in Figure 15(a) that “S” decreases with the increase of the applied depth. PC induced the highest “S” at low applied indentation depth compared to MR7 and CR39. The difference in “S” between the three polymers decreases with the increase of the applied depth until becoming insignificant at Z = 4 µm. On the other hand, CR39 induces a higher “S” than MR7 and this difference is not significantly affected by the variation of the indentation depth.

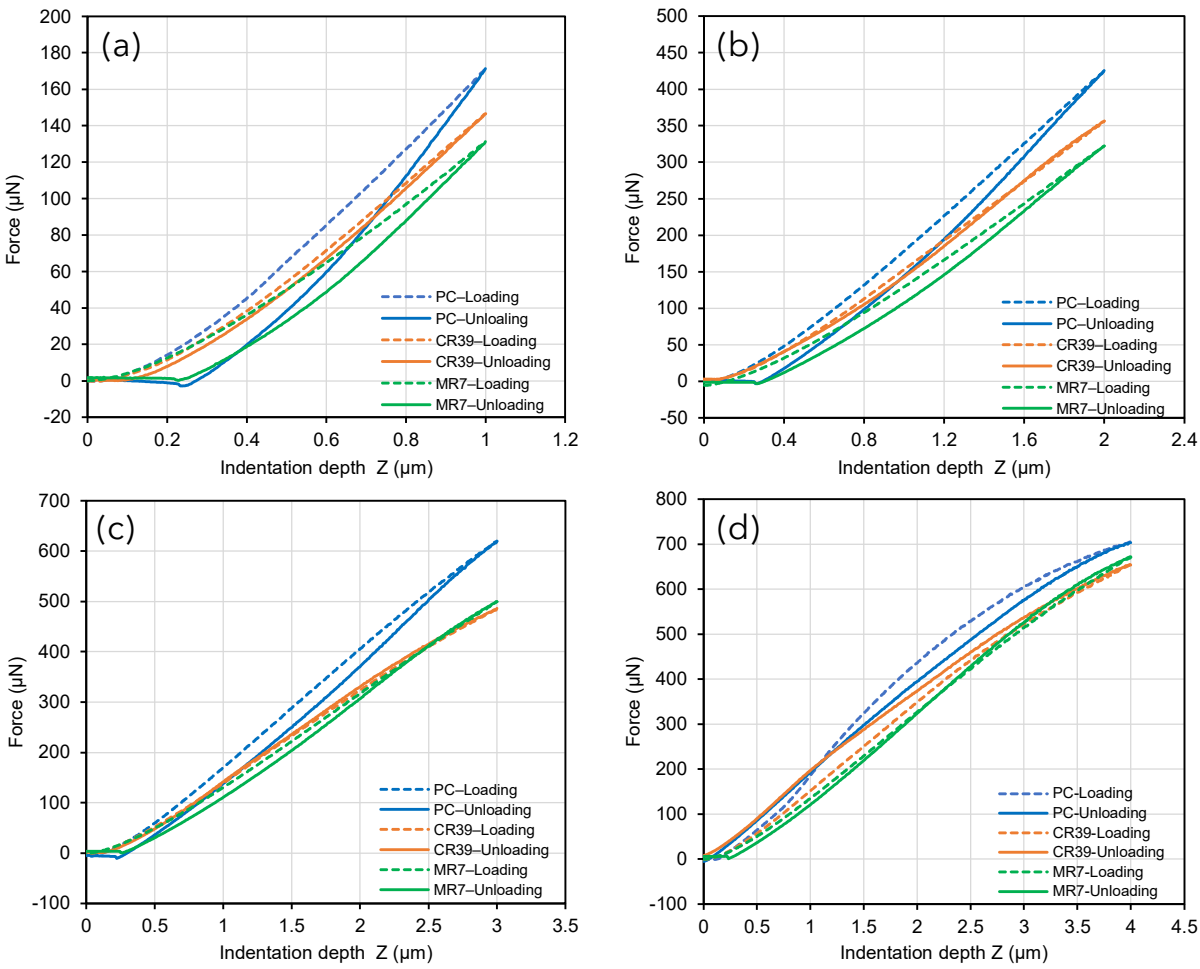

Figure 14: Typical loading-unloading curves obtained from nanoindentation of PC, MR7, and CR39 with indentation depths of (a) 1 µm, (b) 2 µm, (c) 3 µm, and (d) 4 µm.

The results of Figure 15(a) are in good agreement with the experimental observation of the relative spring-back defects induced by orthogonal cutting (section 3.3). Indeed, Figure 15(b) presents the relative slope (ΔS) which is the difference between the average "S" of two polymers. ΔS is then calculated as follows: $\Delta S_{(MR7\text{-}PC)} = S_{(PC)} - S_{(MR7)}$, $\Delta S_{(CR39\text{-}PC)} = S_{(PC)} - S_{(CR39)}$, and $\Delta S_{(MR7\text{-}CR39)} = S_{(CR39)} - S_{(MR7)}$. The results of Figure 15(b) have the same behavior as those presented in Figure 12 for the relative spring-backs: the relative ΔS of MR7-PC shows the highest values, followed by the ΔS of CR39-PC and both show a significant decrease when increasing the applied indentation depth. Nevertheless, MR7-CR39 displays the lowest values of ΔS with no significant effect of the applied indentation depth. The same behavior has been identified in Figure 12 for the relative spring-back of MR7-PC, CR39-PC, and MR7-CR39 hybrid polymer samples.

It can be concluded from the results of nanoindentation analysis that the spring-back behaviors of PC, MR7, and CR39 due to elastic recovery are expressively different and this could probably be the origin of the difference in the relative spring-back defects induced by the micro-machining process.

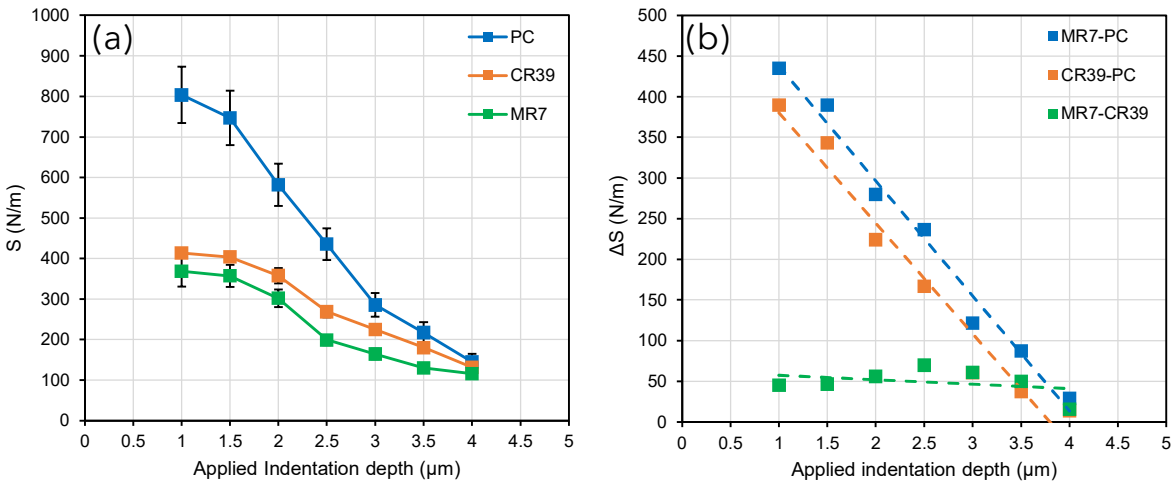

Figure 15: (a) Evolution of the slope "S" of the nanoindentation unloading curves from the maximum force, (b) Evolution of the relative slope "ΔS" of the nanoindentation unloading curves

4. Conclusions

In this paper, a comparative analysis has been conducted to identify the shape defects induced by the micro-machining of optical polymers. The orthogonal cutting configuration has been used to perform the cutting experiments on polycarbonate (PC), Allyl Diglycol Carbonate (CR39), and polythiourethane (MR7) polymers with microscale cutting depth values (from 3 μm to 23 μm). The comparative analysis has been carried out by cutting hybrid samples that are composed of two polymers, and in which one polymer is considered as a reference for the comparison of the surface shape by an optical interferometer. Mechanical characterization at the microscale has been also conducted using nanoindentation to compare the mechanical reaction of each optical polymer and hence explain the cutting behavior. The following conclusions can be drawn:

- PC generates a curled and continuous chip during orthogonal cutting due to its thermoplastic origin (ductile failure), while CR39 produces a fragmented chip in the form of debris due to its thermoset origin (brittle failure). Despite its thermoset origin, MR7 generates a continuous chip because of its high plastic deformation ability revealed by nanoindentation, which is due to its higher chemical molar mass compared to conventional thermoset resins. However, the MR7 chip does not curl due to the damage induced by its lamellar structure revealed by microscopic observations.
- The present study reveals a correlation between the machining thrust forces and the machining-induced shape defects in terms of material spring-back. MR7-PC hybrid samples generate the highest thrust forces that decrease with the increase of the cutting depth. CR39-PC hybrid samples have the same trend in thrust forces with lower values than that of MR7-PC, while thrust forces of MR7-CR39 hybrid

samples show the lowest values without significant effect of the cutting depth. The same thrust forces behavior is identified with the relative spring-back defects of the three hybrid polymer samples. These results demonstrate that the thrust force analysis could be an indicator for predicting the spring-back defects induced by micro-machining.

- The difference in spring-back properties between PC, MR7, and CR39 has been identified by the assessment of the slope of the nanoindentation unloading curves from the maximum indentation force ("S"). MR7 induces the lowest values of "S", while PC generates the highest "S" values that decrease significantly with the increase of the applied indentation depth to be near to those of MR7 and CR39. Calculating the difference in the slopes (ΔS) for the couples MR7-PC, CR39-PC, and MR7-CR39 allows for determining a similar behavior of ΔS to that of the relative spring-back defects. This demonstrates that the spring-back properties of the glassy polymers are probably the cause of the shape defects induced by micro-machining.

The results of this paper should be considered when using micro-machining for the industrial finishing of glassy polymers so the process parameters, such as cutting feed and depth, can be adapted to avoid significant shape defects induced by the material spring-back.

5. References

[1] Schottner, G., Rose, K., and Posset, U., 2003, "Scratch and Abrasion Resistant Coatings on Plastic Lenses - State of the Art, Current Developments and Perspectives," J. Sol-Gel Sci. Technol., **27**(1), pp. 71–79.

[2] Jha, G. S., Seshadri, G., Mohan, A., and Khandal, R. K., 2008, "Sulfur Containing Optical Plastics and Its Ophthalmic Lenses Applications," E-Polymers, **8**(1).

[3] Bauer, T., 2004, "Optical Materials: Plastics," Encycl. Mod. Opt., pp. 480–488.

[4] Mitsui Chemicals, 2020, "History of MR™ and Eyeglass Lenses" [Online]. Available: https://jp.mitsuichemicals.com/en/special/mr/history/. [Accessed: 10-Mar-2023].

[5] Caro, J., Cuadrado, N., González, I., Casellas, D., Prado, J. M., Vilajoana, A., Artús, P., Peris, S., Carrilero, A., and Dürsteler, J. C., 2011, "Microscratch Resistance of Ophthalmic Coatings on Organic Lenses," Surf. Coatings Technol., **205**(21–22), pp. 5040–5052.

[6] Sahoo, P., Patra, K., Singh, V. K., Mittal, R. K., and Singh, R. K., 2020, "Modeling Dynamic Stability and Cutting Forces in Micro Milling of Ti6Al4V Using Intermittent Oblique Cutting Finite Element Method Simulation-Based Force Coefficients," J. Manuf. Sci. Eng. Trans. ASME, **142**(9).

[7] Sahoo, P., and Patra, K., 2021, "Cumulative Reduction of Friction and Size Effects in Micro Milling through Proper Selection of Coating Thickness of TiAlN Coated Tool: Experimental and Analytical Assessments," J. Manuf. Process., **67**, pp. 635–654.

[8] Anand, R. S., Patra, K., and Steiner, M., 2014, "Size Effects in Micro Drilling of Carbon Fiber Reinforced Plastic Composite," Prod. Eng., **8**(3), pp. 301–307.

[9] Gubbels, G. P. H., 2006, "Diamond Turning of Glassy Polymers," Technische Universiteit Eindhoven.

[10] Bolat, M., 2013, "Machining of Polycarbonate for Optical Applications," Middle East Technical University.

[11] Lucca, D. A., Klopfstein, M. J., and Riemer, O., 2020, "Ultra-Precision Machining: Cutting with Diamond Tools," J. Manuf. Sci. Eng. Trans. ASME, **142**(11).

[12] Li, L., Collins, S. A., and Yi, A. Y., 2007, "Optical Effect of Surface Finish by Single Point Diamond Machining," Proc. 22nd Annu. ASPE Meet. ASPE 2007, **132**(2), pp. 0210021–0210029.

[13] Sambhav, K., Tandon, P., Kapoor, S. G., and Dhande, S. G., 2013, "Mathematical Modeling of Cutting Forces in Microdrilling," J. Manuf. Sci. Eng., **135**(1).

[14] Liu, X., DeVor, R. E., and Kapoor, S. G., 2006, "An Analytical Model for the Prediction of Minimum Chip Thickness in Micromachining," J. Manuf. Sci. Eng., **128**(2), pp. 474–481.

[15] Sun, X., and Cheng, K., 2015, "Micro-/Nano-Machining through Mechanical Cutting," *Micromanufacturing Engineering and Technology: Second Edition*, William Andrew Publishing, pp. 35–59.

[16] Mallick, P. S., Pratap, A., and Patra, K., 2022, "Review on Cryogenic Assisted Micro-Machining of Soft Polymer: An Emphasis on Molecular Physics, Chamber Design, Performance Analysis and Sustainability," J. Manuf. Process., **80**, pp.

930–957.

[17] Sahoo, P., Patra, K., Szalay, T., and Dyakonov, A. A., 2020, “Determination of Minimum Uncut Chip Thickness and Size Effects in Micro-Milling of P-20 Die Steel Using Surface Quality and Process Signal Parameters,” Int. J. Adv. Manuf. Technol., **106**(11–12), pp. 4675–4691.

[18] Callister, W. D., and Rethwisch, D. G., 2018, *Materials Science and Engineering: An Introduction*, Wiley, Hoboken, NJ, USA.

[19] Jee, A. Y., and Lee, M., 2010, “Comparative Analysis on the Nanoindentation of Polymers Using Atomic Force Microscopy,” Polym. Test., **29**(1), pp. 95–99.

[20] Mitsui Chemicals, 2012, “MR™ Lens Brochure” [Online]. Available: https://eu.mitsuichemicals.com/sites/default/files/media/document/2018/mr_brochure_en.pdf. [Accessed: 20-Mar-2023].

[21] Ahmad, S., and Stejny, J., 1991, “Polymerisation, Structure and Track Recording Properties of CR-39,” Int. J. Radiat. Appl. Instrumentation. Part, **19**(1–4), pp. 11–16.

[22] Gamardella, F., Ramis, X., De la Flor, S., and Serra, À., 2019, “Preparation of Poly(Thiourethane) Thermosets by Controlled Thiol-Isocyanate Click Reaction Using a Latent Organocatalyst,” React. Funct. Polym., **134**, pp. 174–182.

[23] Desarkar, M., Senthilkumar, P., Franklin, S., and Chatterjee, G., 2012, “Effect of Particulate Fillers on Thermal Expansions and Other Critical Performances of Polycarbonate-Based Compositions,” J. Appl. Polym. Sci., **124**(1), pp. 215–226.

[24] Dixit, M., Mathur, V., Gupta, S., Baboo, M., Sharma, K., and Saxena, N. S., 2009, “Morphology, Miscibility and Mechanical Properties of PMMA/PC Blends,” Phase Transitions, **82**(12), pp. 866–878.

[25] Oliver, W. C., and Pharr, G. M., 1992, “An Improved Technique for Determining Hardness and Elastic-Modulus Using Load and Displacement Sensing Indentation Experiments,” J. Mater. Res., **7**(6), pp. 1564–1583.

[26] Chegdani, F., and El Mansori, M., 2023, “Effect of the Measurement Contact Scale on the Thermomechanical Characterization of Biocomposite Surfaces,” Surf. Topogr. Metrol. Prop., **11**(1), p. 014009.

[27] Bourmaud, A., and Pimbert, S., 2008, “Investigations on Mechanical Properties of Poly(Propylene) and Poly(Lactic Acid) Reinforced by Miscanthus Fibers,” Compos. Part A Appl. Sci. Manuf., **39**(9), pp. 1444–1454.

[28] Sheikh-Ahmad, J. Y., 2009, “Mechanics of Chip Formation,” *Machining of Polymer Composites*, Springer, Boston, MA, pp. 63–110.

[29] Feng, H., Sheng, Y., Chen, G., Jin, B., Fang, Z., Yang, B., Zhou, X., Wu, W., Xie, T., and Zheng, N., 2023, “Ultratough Yet Dynamic Crystalline Poly(Thiourethane) Network Directly from Low Viscosity Precursors,” CCS Chem., pp. 1–11.

[30] Liu, J., Zhao, Z., Wang, W., Mays, J. W., and Wang, S. Q., 2019, “Brittle-Ductile Transition in Uniaxial Compression of Polymer Glasses,” J. Polym. Sci. Part B Polym. Phys., **57**(12), pp. 758–770.

[31] Chen, C., Gnanou, Y., and Feng, X., 2022, “Organocatalytic Selective Coupling of Episulfides with Carbon Disulfide for the Synthesis of Poly(Trithiocarbonate)s and Cyclic Trithiocarbonates,” Polym. Chem., **13**(23), pp. 3471–3478.

[32] “National Center for Biotechnology Information (2024). PubChem Compound Summary for CID 8879, Allyl Diglycol Carbonate” [Online]. Available: https://pubchem.ncbi.nlm.nih.gov/compound/8879. [Accessed: 26-Jan-2024].

[33] "National Center for Biotechnology Information (2024). PubChem Compound Summary for CID 169944, Epoxy Resin" [Online]. Available: https://pubchem.ncbi.nlm.nih.gov/compound/Epoxy-resin. [Accessed: 26-Jan-2024].

[34] Maurotto, A., Siemers, C., Muhammad, R., Roy, A., and Silberschmidt, V., 2014, "Ti Alloy with Enhanced Machinability in UAT Turning," Metall. Mater. Trans. A Phys. Metall. Mater. Sci., **45**(6), pp. 2768–2775.

[35] Shyha, I., Gariani, S., El-Sayed, M. A., and Huo, D., 2018, "Analysis of Microstructure and Chip Formation When Machining Ti-6Al-4V," Metals (Basel)., **8**(3), p. 185.

[36] Ye, G. G., Xue, S. F., Ma, W., and Dai, L. H., 2017, "Onset and Evolution of Discontinuously Segmented Chip Flow in Ultra-High-Speed Cutting Ti-6Al-4V," Int. J. Adv. Manuf. Technol., **88**(1–4), pp. 1161–1174.

[37] Sharma, S., and Meena, A., 2021, "Microstructure Induced Shear Instability Criterion during High-Speed Machining of Ti-6Al-4V," J. Manuf. Sci. Eng. Trans. ASME, **143**(6), pp. 1–25.

[38] Ramalingam, S., and Hazra, J., 1973, "Dynamic Shear Stress—Analysis of Single Crystal Machining Studies," J. Eng. Ind., **95**(4), pp. 939–944.

[39] Rodríguez, J. M., Carbonell, J. M., and Jonsén, P., 2020, "Numerical Methods for the Modelling of Chip Formation," Arch. Comput. Methods Eng., **27**(2), pp. 387–412.